Preprints (www.preprints.org) | NOT PEER-REVIEWED | Posted: 3 April 2018 doi:10.20944/preprints201804.0036.v1

Peer-reviewed version available at Materials 2018, 11, 1030; doi:10.3390/ma11061030

Degradation of methylene blue dye in the presence of visible light using SiO_2@α-Fe_2O_3 nanocomposites deposited on SnS_2 flowers

Sridharan Balu[1], Kasimayan Uma[2*], Guan-Ting Pan[1], Thomas C.-K. Yang[1,2*] Sayee Kannan Ramaraj[3]

[1]Department of Chemical Engineering and biotechnology, National Taipei University of Technology, Taipei, Taiwan 106, bsridharanbsc.12@gmail.com (S.B.); t6679013@gmail.com (G.T.P.); ckyang@mail.ntut.edu.tw (T.C.K.Y.)
[2] Precision Analysis and Research Center, National Taipei University of Technology, Taipei, Taiwan 106, umamahesh16@gmail.com (K.U.)
[3]PG & Research Department of Chemistry, Thiagarajar College, Madurai-625009, Tamilnadu, India, sayeekannanramaraj@gmail.com (S.K.R.)
* Correspondence: ckyang@mail.ntut.edu.tw

Abstract: Semiconductor materials have been shown to have better photocatalytic behavior and can be utilized for the photodegradation of organic pollutants. In this work, three-dimensional flower-like SnS_2 were synthesized by a facile hydrothermal method. Core-shell structured SiO_2@α-Fe_2O_3 nanocomposites were then deposited on the top of the SnS_2 flowers. The as-synthesized nanocomposites were characterized by X-ray diffraction (XRD), Raman spectroscopy, field emission scanning electron microscopy (FE-SEM), Brunauer-Emmett-Teller (BET) and photoluminescence spectroscopy (PL). The photocatalytic behavior of the SnS_2-SiO_2@α-Fe_2O_3 nanocomposites was observed by observing the degradation of methylene blue (MB). The results show an effective enhancement of photocatalytic activity for the degradation of MB especially for the 15 wt. % SiO_2@α-Fe_2O_3 nanocomposites on SnS_2 flowers.

Keywords: Photocatalyst, Flower-like SnS_2, Nanocomposites, Visible light, Methylene blue

1. Introduction

Environmental pollution is primarily caused by the willful disposal of waste and toxic pollutants without proper treatment. Increasingly, this leads to soil and water pollution, and is very deleterious to human health [1, 2]. In order to avoid this issue, a variety of processes have been adopted to remove pollutants from wastewater, including adsorption [3], oxidation [4], reduction, and flocculation [5]. Among these various methods, photocatalysis and green technology have shown good potential for the removal of organic pollutants [6-8]. It has been reported that a number of semiconductors can be used to degrade a variety of organic pollutants under the irradiation of light with different wavelengths [9, 10].

There are several semiconductor materials which have been used for the promotion of a photocatalytic activity. Among these, the eco-friendly iron oxide (α-Fe_2O_3) nanomaterials exhibit favorable photocatalytic activity [11] due to their high specific surface area and high crystallinity with the additional advantage of being low cost [12, 13]. Hematite (α-Fe_2O_3) is the most stable iron oxide under ambient conditions, and due to its narrow band gap, can act as a visible light photocatalyst [14]. This makes α-Fe_2O_3 a good potential candidate for irradiation by visible light which enhances the efficiency of the solar light [9]. Nowadays, many researchers have tried to improve the photocatalytic behavior of Fe_2O_3 by coupling it with different semiconductor metal oxide nanoparticles, nano tubes and nano flowers [15, 16].

The metal sulfide semiconductors [17] like SnS_2 usually have high light absorbing capabilities in the visible and shorter wavelengths near the IR regions [18]. SnS_2 has also been used as an n-type semiconductor because of having a low band gap value of 2.2 eV [19] and high electrical conductivity which mean that it can act as a catalyst, for example in lithium-ion batteries [20]. Tin sulfide is also widely used as an energy material due to its simple binary composition and the abundance of tin and sulfur [21, 22]. It is often used in research

© 2018 by the author(s). Distributed under a Creative Commons CC BY license.

Preprints (www.preprints.org) | NOT PEER-REVIEWED | Posted: 3 April 2018 doi:10.20944/preprints201804.0036.v1

Peer-reviewed version available at Materials 2018, 11, 1030; doi:10.3390/ma11061030

because of its unique physicochemical properties which give it low toxicity, good chemical stability and it is inexpensive [23]. In addition, with its unique multilayer flower-like structure, SnS_2 exhibits superior photocatalytic degradation of methylene blue (MB) under visible light [24].

Here, SiO_2 shells were used to maintain the structure of the nanocomposites and also avert their aggregation during the photocatalytic reactions [25, 26]. This is the very important to ensure the imperishability of the photocatalyst [27]. The preference of SiO_2 for the inner core is based on the following two considerations: first, the silica nanospheres can produce multiple reflections of the visible light irradiated into the internal cavity; [28] second, the well-ordered and smooth structure of SiO_2 can promote the transfer of dye molecules to the semiconductor material [29, 30].

Here, we report a facile approach for the synthesis of SnS_2-SiO_2@α-Fe_2O_3 nanocomposites by means of the hydrothermal method. The photocatalytic activity of SnS_2-SiO_2@α-Fe_2O_3 nanocomposites was examined for the degradation of methylene blue (MB) under irradiation by visible light. Additionally, samples with different weight percentages of SiO_2@α-Fe_2O_3 on the SnS_2 flowers were studied to find the ideal ratio for the best photocatalytic activity.

2. Experimental Procedure

2.1. Materials used

Tin (IV) chloride pentahydrate (98%, Sigma Aldrich), Thioacetamide (TAA 99%, Acros), Isopropyl Alcohol (Tedia), Ethanol (99%, Fisher Chemicals), tetraethylorthosilicate (TEOS 95%, Acros), ammonia solution (Choneye Pure Chemicals), iron (III) chloride hexahydrate and methylene blue (MB) were used. All the above reagents were analytical grade without any additional purification. Deionized water was used throughout the reactions and synthesis process.

2.2. Synthesis of flower-like SnS_2

SnS_2 flowers were prepared through a facile hydrothermal method using the same procedure as reported previously [31]. The procedure for the synthesis of the SnS_2 flowers is as follows: 0.45g $SnCl_4.5H_2O$ and 0.33 g thioacetamide (TAA) were dissolved in 30mL isopropyl alcohol. After 30 minutes of vigorous stirring, the solution was transferred to a Teflon-lined stainless-steel autoclave with a volume of 50 mL and then transferred to a muffle furnace followed by hydrothermal treatment at 180 °C for 24 hours. The golden coloured precipitates were then centrifuged and rinsed with copious amounts of deionized water and ethanol before being dried in a vacuum for 12 hours at 80 °C.

2.3. Synthesis of SiO_2@α-Fe_2O_3 composite spheres

In this experiment, silica spheres were synthesized using the same procedure described in our previous work [32]. A mixture of tetraethyl orthosilicate (TEOS) (5 mL), anhydrous ethanol (25 mL), and (5 mL) water was stirred at room temperature for 30 minutes, followed by the addition of 1 mL of ammonia solution. 15 mL of anhydrous ethanol were then added to the above mixture which was stirring for 12 hours at room temperature. After centrifugation, the SiO_2 was collected and washed several times with water and ethanol. Finally, the obtained SiO_2 spheres were dried in a vacuum oven at 60°C for 12 hours. Using ultrasonication, 100 mg of SiO_2 spheres were uniformly dispersed in 40 mL of water, followed by the addition of 50 mg iron (III) chloride hexahydrate and 30 mg urea. The mixture was continuously stirred at 95 °C for 6 hours. The FeOOH-coated

Preprints (www.preprints.org) | NOT PEER-REVIEWED | Posted: 3 April 2018 doi:10.20944/preprints201804.0036.v1

Peer-reviewed version available at Materials 2018, 11, 1030; doi:10.3390/ma11061030

SiO_2 spheres were separated by centrifugation and then washed several times with water and ethanol. Finally, the spheres were dried in a vacuum oven at 60 °C for 12 hours. The resulting FeOOH-coated SiO_2 composite spheres were calcined at 450°C for 4 hours to get crystalline α-Fe_3O_4 nano particles.

2.4. Preparation of SnS_2- SiO_2@α-Fe_2O_3 nanocomposites

The SnS_2-SiO_2@α-Fe_2O_3 (SSF) nanocomposites were prepared by adding 100 mg of flower-like SnS_2 and different weight ratios (5, 10, 15, 20, 25 mg) of SiO_2@α-Fe_2O_3 nanocomposites at 70 °C followed by effective stirring for 6 hours. The resultant product obtained by centrifugation was then washed with ethanol and water. The obtained products were labelled SSF-X=5, 10, 15, 20, 25 wt. % corresponding to the weight ratio of the SiO_2@α-Fe_2O_3 nanocomposites.

2.5. Degradation of methylene blue (MB) dye

The as-synthesized SnS_2-SiO_2@α-Fe_2O_3 (SSF-15 wt. %) nanocomposites (40 mg) were dispersed in 100 mL of 5ppm MB dye solution and stirred at 30 min in the dark. The reaction dye solution was then irradiated under visible light (410 nm). A 5 ml sample was taken every 15 minutes and the degradation was monitored by using UV-vis spectroscopy. The proceeding degradation of MB obtained by using α-Fe_2O_3, SnS_2 and SiO_2@α-Fe_2O_3 was observed to check on the photocatalytic activity.

2.6. Characterization

The X-Ray diffraction studies were carried out using the Cu-K_α line XRD, on a PANanalytical X'Pert PRO instrument. The FTIR experiment was carried out using a PerkinElmer, FT-IR Spectrometer Frontier in the range between 400 and 4000 cm^{-1}. The structure and morphology of the catalysts were analyzed using FE-SEM JEOL JSM-7100F. The surface area of the as-synthesized nanocomposites was obtained by BET using Micromeritics-Gemini V, ASAP 2020. Photoluminescence studies were carried out using a PL Spectrometer, Dongwoo - Ramboss 500i. The electrochemical impedance spectroscopy (EIS) was carried out using a Zive Potentiostat, SP100.

3. Results and discussion

3.1. X-Ray diffraction

The crystalline nature of the obtained samples was confirmed by XRD. The XRD results for the as-prepared SnS_2 and SnS_2-SiO_2@α-Fe_2O_3 (SSF-X) [X=5, 10, 15, 20 and 25 wt. %] are shown in figure 1.The inset to the figure shows the set of peaks at 28.29°, 32.2°, 41.8°, 50.1°, 52.5° and 55.2° which can be indexed to the pure hexagonal phase of SnS_2 as confirmed by JCPDS 75-0367 [33]. After the addition of various concentrations of SiO_2@α-Fe_2O_3 to the SnS_2 flowers, the intensity of the SnS_2 decreased due to the deposition of the SiO_2@α-Fe_2O_3 nanocomposites. Figure 1 clearly shows the 2θ peak at 32.2° that corresponds to the (011) diffraction planes indexed to the (011) crystalline SnS_2 which decreased with an increase in the concentration of the SiO_2@α-Fe_2O_3 nanocomposites on SnS_2, confirming the deposition of SiO_2@α-Fe_2O_3 nanocomposites.

Preprints (www.preprints.org) | NOT PEER-REVIEWED | Posted: 3 April 2018 doi:10.20944/preprints201804.0036.v1

Peer-reviewed version available at Materials 2018, 11, 1030; doi:10.3390/ma11061030

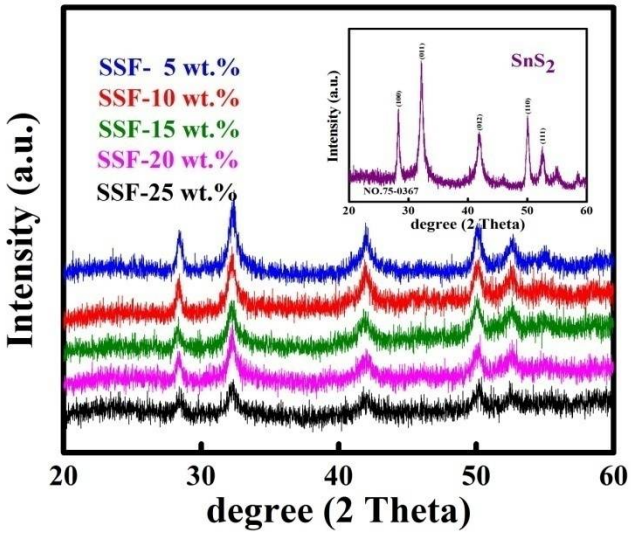

Figure 1. XRD patterns for SnS_2-SiO_2@α-Fe_2O_3 nanocomposites with different concentrations (SSF-5, 10, 15, 20 and 25 wt. %). The inset shows the XRD pattern for as-synthesized flower-like SnS_2.

3.2. FE-SEM Structure

The structural morphologies of SnS_2, α-Fe_2O_3 and SnS_2-SiO_2@α-Fe_2O_3 (SSF-X) [X=5, 10, 15, 20 and 25 wt. %] were studied using FE-SEM. The flower-like morphology of the as-prepared SnS_2 can be clearly observed in the FE-SEM images. This morphology is produced by the accumulation of several nanosheets assembled at one solitary point. Interestingly, the uniform nanosheet morphology is mainly caused by the intrinsic anisotropic growth of SnS_2 crystals [31]. The size of each nanosheet is about 20 nm and the size of the full flower-like structure is in the range between 3 and 4 μm, as shown in Figure 2(a). In the SnS_2-SiO_2@α-Fe_2O_3 composites, α-Fe_2O_3 nanoparticles are deposited on the surface of SiO_2 spheres with a size of around 150 nm, as shown in Figure 2(b). The SiO_2@α-Fe_2O_3 nanocomposites rest on the surface of the SnS_2 flowers, as shown in Figure 2(c). The SiO_2 core-shell structure allows the multiple reflections of visible light, and the α-Fe_2O_3 and SnS_2 are used to enhance the absorbance sites. EDX observations confirmed the presence of SnS_2-SiO_2@α-Fe_2O_3 composites. The EDX results give energy peaks congruent with the elements of Sn, S, Fe, O, and Si in Figure 2(d).

Preprints (www.preprints.org) | NOT PEER-REVIEWED | Posted: 3 April 2018 doi:10.20944/preprints201804.0036.v1

Peer-reviewed version available at Materials 2018, 11, 1030; doi:10.3390/ma11061030

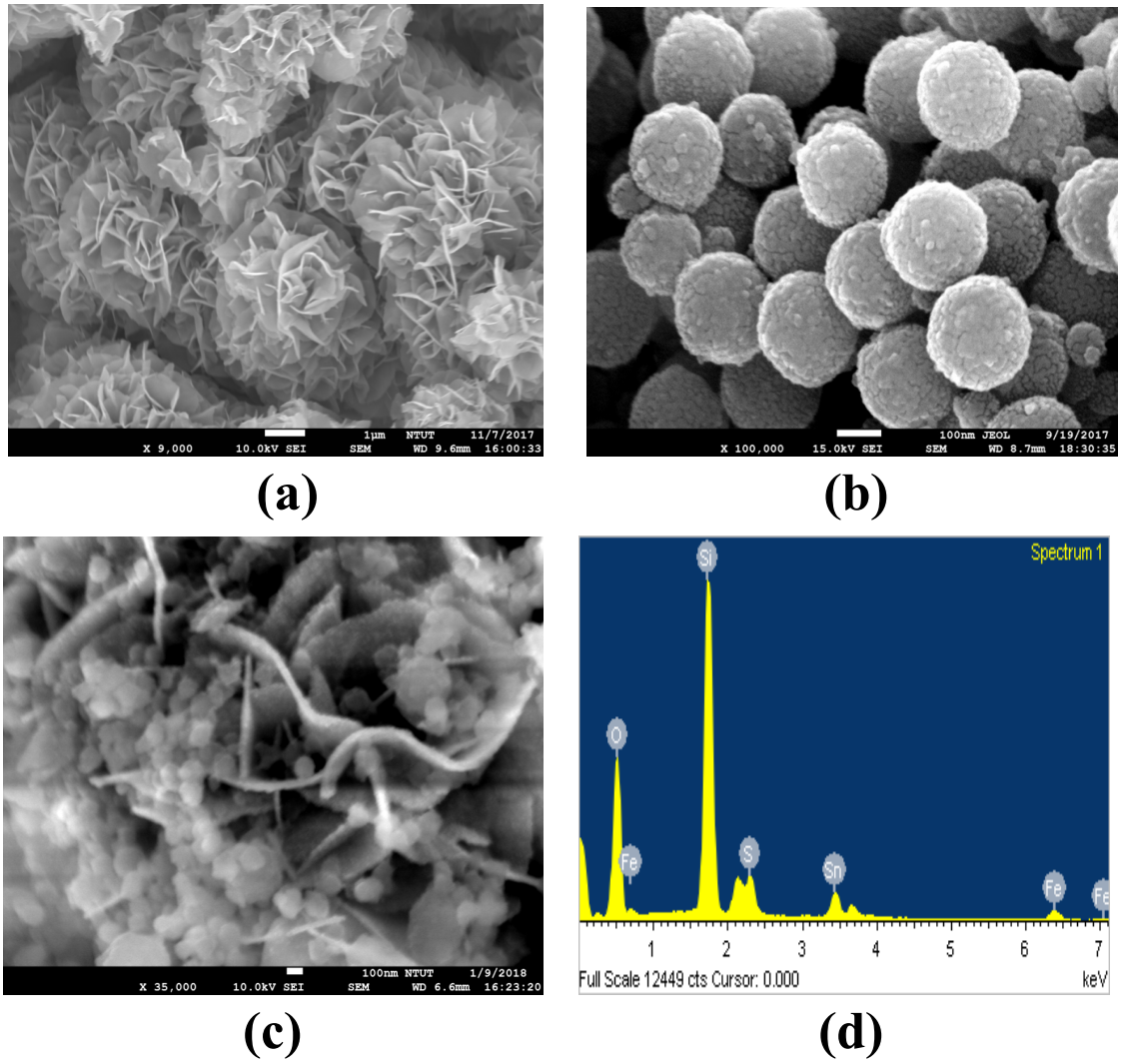

Figure 2. FE-SEM images of (a) Flower-like SnS_2, (b) SiO_2@α-Fe_2O_3 nanocomposites (c) SnS_2-SiO_2@α-Fe_2O_3 nanocomposite and (d) EDX spectra corresponding to SnS_2-SiO_2@α-Fe_2O_3 nanocomposite.

3.3. EIS Spectra

The EIS spectra were obtained for the different SnS_2-SiO_2@α-Fe_2O_3 (SSF-X) [X=5, 10, 15, 20 and 25 wt. %] nanocomposite samples with a modified glassy carbon electrode (GCE) for the KCl (0.1 M) containing 5 mM of $[Fe(CN)_6]^{3-}$and $[Fe(CN)_6]^{4-}$. This EIS spectrum shows the electrical and interfacial properties of the aforementioned nanocomposite materials. The SSF-15 wt. % nanocomposite produces a smaller semi-circle in comparison to the other composites. In Figure 3, the smallest semi-circle, with the reduced diameter, indicates very low resistance. The electron transfer resistance observed is 154,149, 150, 145, and 101 $k\Omega^{-1}$ for the various-25, 20, 15, 10 and 5 wt. % composites, respectively. The low resistance observed for the SSF-15 wt. % nanocomposite is due to the counterpart (stoichiometric) ratio between SnS_2 and SiO_2@α-Fe_2O_3. The deposition of SiO_2@α-Fe_2O_3 on the SnS_2 flowers plays an important role in enhancing the charge resistance due to the low specific capacity of the nanocomposites. This increased electrical conductivity can also extend the lifespan of the charge carriers, as well as increase the reduction in the electron-hole recombination rate. It is also worth mentioning that higher impedance values are observed for the 15wt. % of SiO_2@α-Fe_2O_3 nanocomposites than for all of the other nanocomposites.

Preprints (www.preprints.org) | NOT PEER-REVIEWED | Posted: 3 April 2018 doi:10.20944/preprints201804.0036.v1

Peer-reviewed version available at Materials 2018, 11, 1030; doi:10.3390/ma11061030

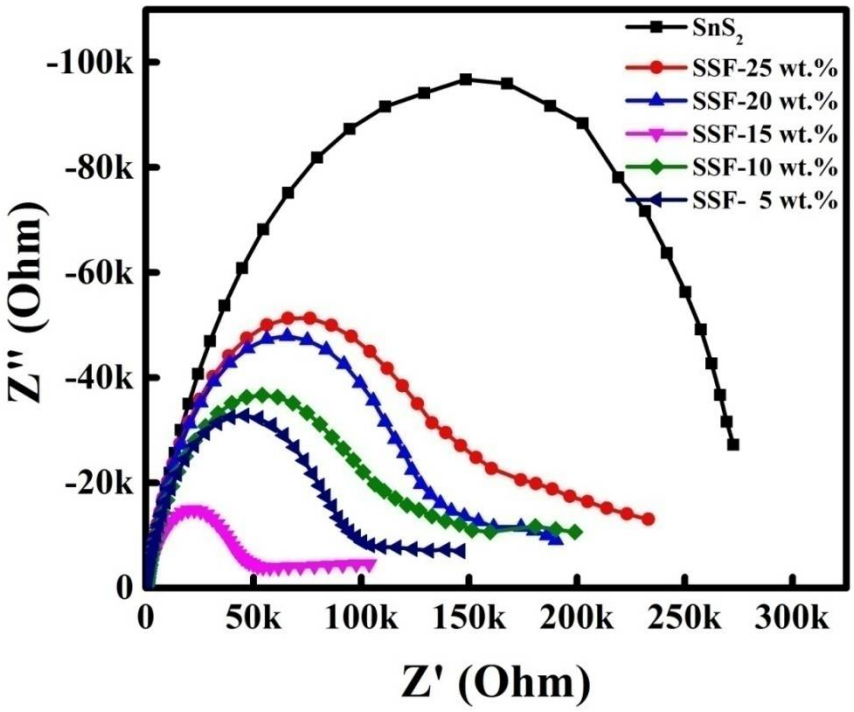

Figure 3. EIS spectra of SnS_2 and different concentrations of SSF-X nanocomposites (X=5, 10, 15, 20 and 25 wt. %)

3.4. FTIR Spectra

The FTIR spectra of the SnS_2 flowers, SiO_2 spheres, and α-Fe_2O_3 and SnS_2-SiO_2@α-Fe_2O_3 nanocomposites are shown in Figure 4. The inset to the figure shows the distinctive peaks at 1535 cm^{-1} and 1657 cm^{-1} representative of the SnS_2. The strong stretching vibration of Si-O-Si at 1111 cm^{-1}, the symmetric vibration of the Si-O-Si at 800 cm^{-1}, and the symmetric stretching vibration of the Si-OH bond at 956 cm^{-1} and 3246 cm^{-1}can be observed. An absorption peak in the range between 3245 and 3450 cm^{-1} appears for all the samples after they have been annealed at 450 °C due to the stretching vibration of the OH band, which indicates the presence of the –OH group [34]. As the percentage of SnS_2 increases from low to higher, there is not much variation in the FTIR spectra. However, the stretching vibrations which are observed for all the samples confirm the presence of OH groups. The bands observed at 474 cm^{-1} and 572 cm^{-1} are due to the Fe-O metal oxide stretching vibration modes and the peak at 1052 cm^{-1} indicates the presence of the Fe-OH group.

Preprints (www.preprints.org) | NOT PEER-REVIEWED | Posted: 3 April 2018 doi:10.20944/preprints201804.0036.v1

Peer-reviewed version available at Materials 2018, 11, 1030; doi:10.3390/ma11061030

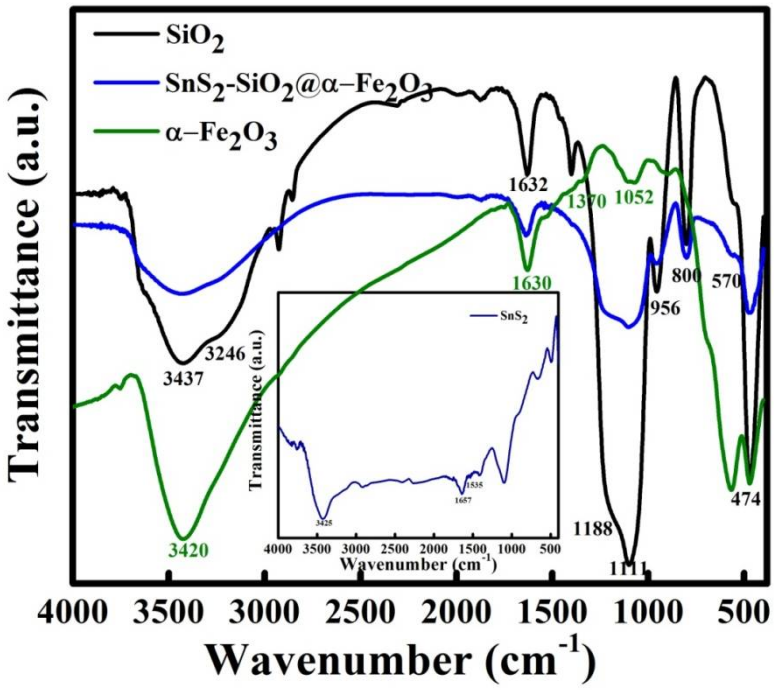

Figure 4. FTIR spectra of SiO_2, α-Fe_2O_3, SnS_2-SiO_2@α-Fe_2O_3 composites; inset shows the SnS_2 spectra

3.5. Raman Spectroscopy

Figure 5 shows the Raman spectra for the SnS_2-SiO_2@α-Fe_2O_3 (SSF-X) [X=5, 10, 15, 20 and 25 wt. %] nanocomposites observed in the range of 100 to 1000 cm^{-1}. The Raman spectrum for SnS_2 exhibits an intense peak at about 315 cm^{-1} which is attributed to the $A1_g$ mode [35, 36]. Increasing the concentration of SiO_2@α-Fe_2O_3 produces no change in the SnS_2 flower-like structure, as shown in Figure 5.

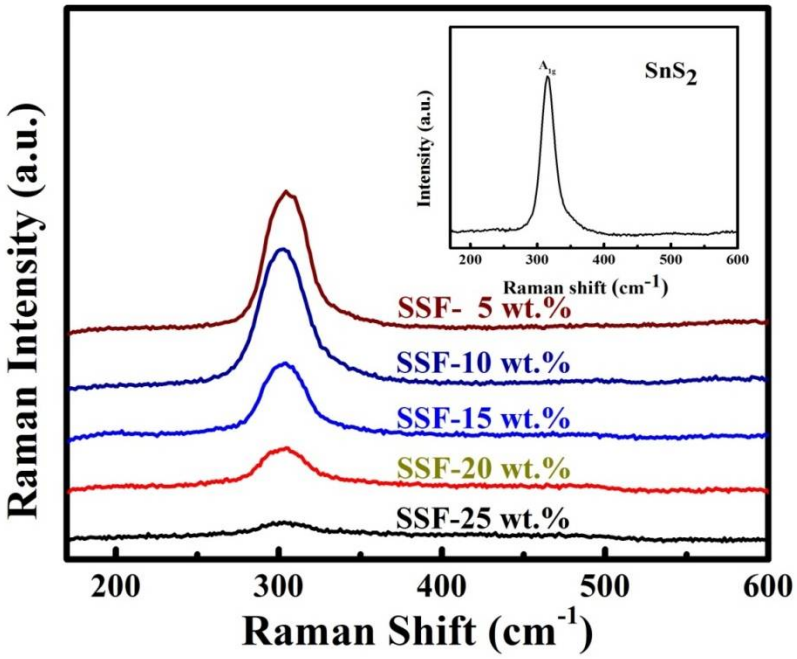

Figure 5. (a) Raman spectra of SnS_2-SiO_2@α-Fe_2O_3 nanocomposites with various concentrations (SSF-5, 10, 15, 20 and 25 wt. %); inset shows the Raman spectra of flower-like SnS_2.

Preprints (www.preprints.org) | NOT PEER-REVIEWED | Posted: 3 April 2018 doi:10.20944/preprints201804.0036.v1

Peer-reviewed version available at Materials 2018, 11, 1030; doi:10.3390/ma11061030

3.6. BET Surface

The surface areas of the as-synthesized SnS_2-SiO_2@α-Fe_2O_3 (SSF-X) [X=5, 10, 15, 20 and 25 wt. %] composites are characterized by nitrogen adsorption-desorption Brunauer Emmett-Teller, as shown in Table 1. From the results of BET analysis, the specific surface areas of SSF-X (X= 5, 10, 15, 20 and 25 wt. %) are calculated to be 41.61, 39.41, 42.8, 41.93 and 40.47 m^2/g, respectively. From the above results, it can be seen that the surface area of SSF-15 is slightly higher among the all specimen. This implies that the enhancement of the adsorption capacity occurred in SSF-15 compare to that of the plain SnS_2 flowers.

Table 1. BET Surface areas of various SnS_2-SiO2@α-Fe2O3 (SSF-X) [X=5, 10, 15, 20 and 25 wt. %] nanocomposites

Sample	BET Surface Area
SnS_2 flowers	41.88 m^2/g
SSF- 5 wt. %	41.61 m^2/g
SSF-10 wt. %	39.41 m^2/g
SSF-15 wt. %	**42.82 m^2/g**
SSF-20 wt. %	41.93 m^2/g
SSF-25 wt. %	42.47 m^2/g

3.7. PL Measurement

Figure 6, shows the PL spectra of SnS_2-SiO_2@α-Fe_2O_3 (SSF-X) [X=5, 10, 15, 20 and 25 wt. %] nanocomposites. The board peak at 600 nm indicates the emission band of SnS_2 flower-like structure. After deposition of various concentration of SiO_2@α-Fe_2O_3 nanocomposites on SnS_2, the peak at 600 nm is decreased, indicating the reduction of recombination rate of electron-hole pairs. The SSF-15 wt. % shows minimum intense PL spectra and demonstrating the efficient charge separation of the composites as shown in Figure 6. This lower excitonic of PL intensity is due to the stronger capacity of dopants to capture photo-induced electrons, higher the separation rate of photoinduced electrons and holes, and higher the photocatalytic activity. Further, the decrease in the light emission intensity indicates the direct radiative recombination and lower recombination of generated carriers. This result shows that the significant reduction in the recombination rate of photogenerated electron-hole pairs are observed in SSF-15 wt. % when compared with other nanocomposites.

Preprints (www.preprints.org) | NOT PEER-REVIEWED | Posted: 3 April 2018 doi:10.20944/preprints201804.0036.v1

Peer-reviewed version available at Materials 2018, 11, 1030; doi:10.3390/ma11061030

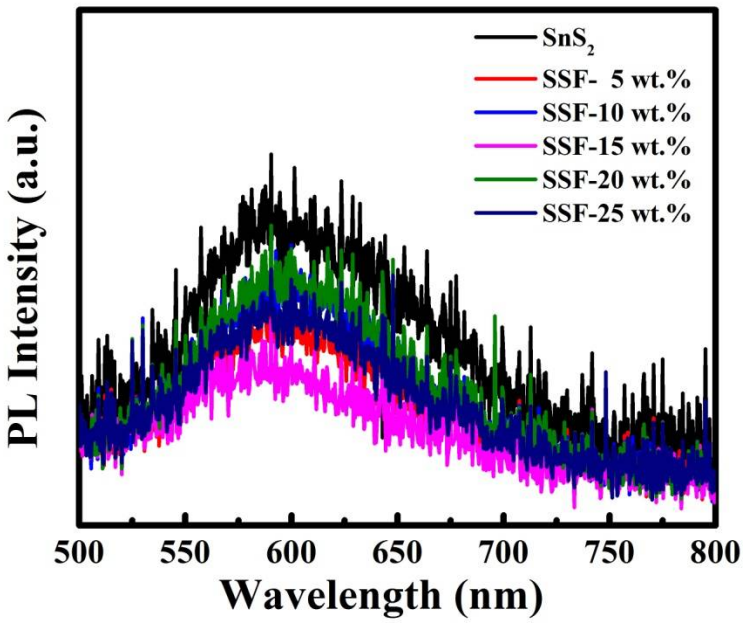

Figure 6. Photoluminescence spectra of SnS_2-SiO_2@α-Fe_2O_3 nanocomposites with different weight percentages (SSF-X) [X=5, 10, 15, 20 and 25 wt. %]

3.8. Dye degradation

Figures 7 (a) and (b) show the process of MB dye degradation after exposure to visible light irradiation in the presence of SnS_2 and SnS_2-SiO_2@α-Fe_2O_3 (SSF-15 wt. %) photocatalysts. The UV-visible absorption spectrum shows a peak at 663 nm as was observed for the MB dye in Figures 7 (a) and (b). When irradiation time was increased, the absorption intensity of the peak at 663 nm decreased, which confirms the progress in the degradation of the MB dye used as a synthesized photocatalyst. For the 15 wt. % SnS_2-SiO_2@α-Fe_2O_3 sample, complete degradation of the MB dye that took only 100 min. Figure 8 shows the percentage of MB dye remaining in the solutions for the SnS_2, Fe_2O_3, SiO_2@Fe_2O_3 and SiO_2@α-Fe_2O_3 nanocomposites under visible light irradiation. Dye degradation of 19, 42, 48 and 96 % were observed for the α-Fe_2O_3, SnS_2, and SiO_2@α-Fe_2O_3 nanocomposites, respectively, at 100 min.

Preprints (www.preprints.org) | NOT PEER-REVIEWED | Posted: 3 April 2018 doi:10.20944/preprints201804.0036.v1

Peer-reviewed version available at Materials 2018, 11, 1030; doi:10.3390/ma11061030

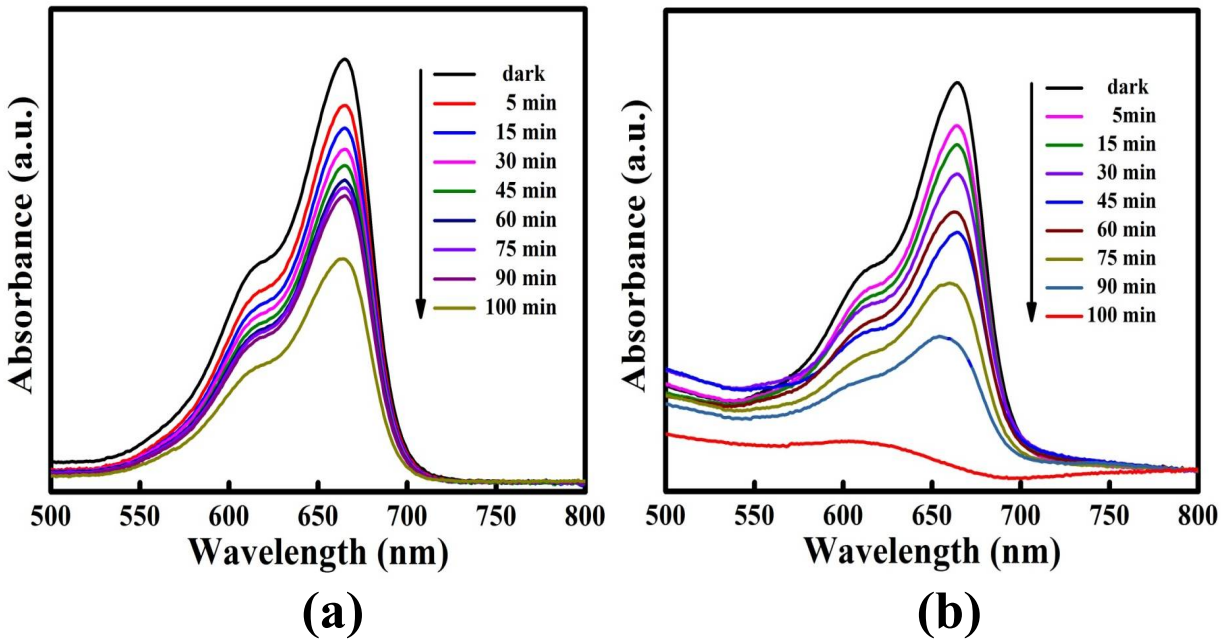

Figure 7. Photodegradation of Methylene blue (MB) dye in aqueous solution under visible light for (a) SnS_2 and (b) SnS_2-SiO_2@α-Fe_2O_3 (SSF-15 wt. %) nanocomposites.

The enhancement of the photocatalytic activity of SnS_2-SiO_2@α-Fe_2O_3 (SSF-15 wt. %) photocatalyst could be explained by two reasons. First, the nanocomposites are prepared by a hydrothermal method having the higher surface area as confirmed by BET. Secondly, SSF-15 wt. % has very lower impedance value in EIS Nyquist plot. Here, the SiO_2 spheres act as large adsorption sites and good locations for α-Fe_2O_3 nanoparticles to absorb the dye molecules. During the photocatalytic reaction, the SnS_2 and α-Fe_2O_3 act as photoactive centers and need a strong interaction between the dye and the surface of the catalyst for the effective degradation of dye [17, 37]. Furthermore, the CB of α-Fe_2O_3 is slightly more negative while the VB is much more positive than that of SnS_2. This leads to increase the driving force of holes migration when compared to electron transfer. Therefore, the efficient charge separation may occur through the strong interfacial interaction in the SnS_2/SiO_2@α-Fe_2O_3 heterostructures, reducing the photogenerated charge recombination rate and therefore improving the photocatalytic activity. The α-Fe_2O_3 nanoparticles used to trap the more electrons which enhances the photocatalytic activity. Due to the reaction between these trapped electrons and dissolved oxygen in the system, the superoxide radical anions ($\bullet O_2^-$) are formed which in turn result information of hydroxyl radicals (•OH). These •OH radicals are mainly responsible for the oxidation of the organic compounds. This mechanism can be observed in terms of the active surface sites on the catalyst surface and the contact area of the dye and the catalyst. The 15 wt. % concentration in SiO_2@α-Fe_2O_3 nanocomposites increases the amount of active sites, which in turn increases the number of hydroxyls (•OH) and superoxide ($\bullet O_2^-$) radicals. Furthermore, the degradation efficiency is reduced when the concentration of nanocomposites exceeds the normal range. This may be due to the agglomeration of the nanocomposites which reduces the penetration of light as well as the absorbance of the dye and the catalyst.

Preprints (www.preprints.org) | NOT PEER-REVIEWED | Posted: 3 April 2018 doi:10.20944/preprints201804.0036.v1

Peer-reviewed version available at Materials 2018, 11, 1030; doi:10.3390/ma11061030

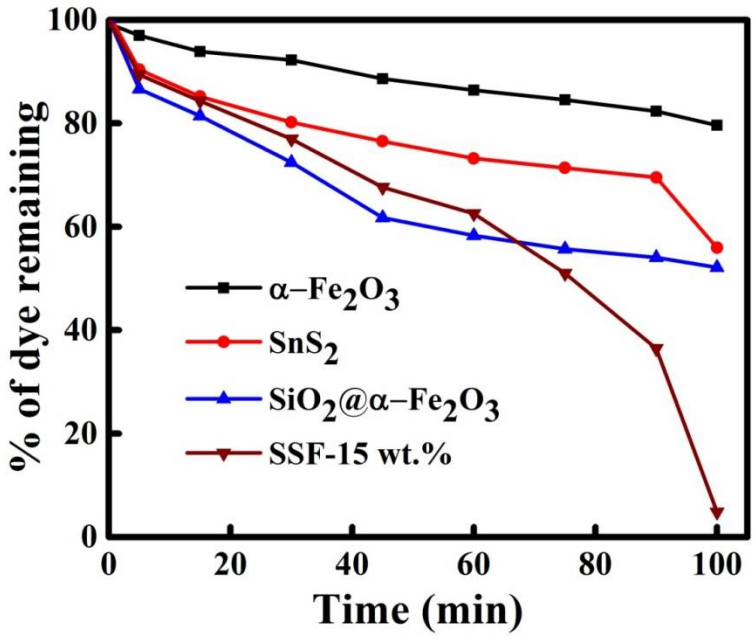

Figure 8. Percentage of degradation and the remaining dye with respect to the different intervals of time in the presence of the photocatalyst α-Fe_2O_3/SnS_2/SiO_2@α-Fe_2O_3/SnS_2-SiO_2@α-Fe_2O_3 under irradiation by visible light.

4. Conclusion

Flower-like SnS_2 and SnS_2-SiO_2@α-Fe_2O_3 nanocomposites with different weight percentages were successfully synthesized by a simple hydrothermal method. The as-prepared nanocomposite enhanced the amount of adsorption of cationic dye (MB) molecules by the addition of SiO_2@α-Fe_2O_3 composites on the SnS_2 flowers, thereby increasing the photocatalytic degradation activity. Due to the simplicity of preparation, it is possible to produce a very low-cost photocatalyst whose higher activity and stability make it a good candidate material for applications in environmental purification.

Acknowledgment

The author would like to thank the Precision Analysis and Research Center, National Taipei University of Technology, Taipei, for their financial support of this research.

References

1. Ahmad, A., et al., *Recent advances in new generation dye removal technologies: novel search for approaches to reprocess wastewater.* RSC Advances, 2015. **5**(39): p. 30801-30818.
2. Gordon, P.F. and P. Gregory, *Organic chemistry in colour*. 2012: Springer Science & Business Media.
3. Ali, I., M. Asim, and T.A. Khan, *Low cost adsorbents for the removal of organic pollutants from wastewater.* Journal of environmental management, 2012. **113**: p. 170-183.
4. Panizza, M. and G. Cerisola, *Removal of organic pollutants from industrial wastewater by electrogenerated Fenton's reagent.* Water Research, 2001. **35**(16): p. 3987-3992.
5. Soltani, N., et al., *Visible light-induced degradation of methylene blue in the presence of photocatalytic ZnS and CdS nanoparticles.* International journal of molecular sciences, 2012. **13**(10): p. 12242-12258.
6. Huang, J., et al., *Facile synthesis of porous TiO2 nanospheres and their photocatalytic properties.* Superlattices and Microstructures, 2015. **81**: p. 16-25.
7. Karimi, L., S. Zohoori, and M.E. Yazdanshenas, *Photocatalytic degradation of azo dyes in aqueous solutions under UV irradiation using nano-strontium titanate as the nanophotocatalyst.* Journal of Saudi Chemical Society, 2014. **18**(5): p. 581-588.

Preprints (www.preprints.org) | NOT PEER-REVIEWED | Posted: 3 April 2018 doi:10.20944/preprints201804.0036.v1

Peer-reviewed version available at Materials 2018, 11, 1030; doi:10.3390/ma11061030

8. Habib, M.A., et al., *Photocatalytic decolorization of brilliant golden yellow in TiO2 and ZnO suspensions.* Journal of Saudi Chemical Society, 2012. **16**(4): p. 423-429.
9. Huang, Y., et al., *Facile synthesis of α-Fe2O3 nanodisk with superior photocatalytic performance and mechanism insight.* Science and technology of advanced materials, 2015. **16**(1): p. 014801.
10. Chen, C., W. Ma, and J. Zhao, *Semiconductor-mediated photodegradation of pollutants under visible-light irradiation.* Chemical Society Reviews, 2010. **39**(11): p. 4206-4219.
11. Barroso, M., et al., *The role of cobalt phosphate in enhancing the photocatalytic activity of α-Fe2O3 toward water oxidation.* Journal of the American Chemical Society, 2011. **133**(38): p. 14868-14871.
12. Liu, X., et al., *Facile synthesis of porous Fe2O3 nanorods and their photocatalytic properties.* Journal of Saudi Chemical Society, 2015. **19**(5): p. 479-484.
13. Mor, G.K., et al., *Vertically oriented Ti− Fe− O nanotube array films: toward a useful material architecture for solar spectrum water photoelectrolysis.* Nano letters, 2007. **7**(8): p. 2356-2364.
14. Klahr, B., et al., *Water oxidation at hematite photoelectrodes: the role of surface states.* Journal of the American Chemical Society, 2012. **134**(9): p. 4294-4302.
15. Hassena, H., *Photocatalytic degradation of methylene blue by using Al2O3/Fe2O3 nano composite under visible light.* Modern Chemistry & Applications, 2016.
16. Pal, B., M. Sharon, and G. Nogami, *Preparation and characterization of TiO2/Fe2O3 binary mixed oxides and its photocatalytic properties.* Materials Chemistry and Physics, 1999. **59**(3): p. 254-261.
17. Zhang, Y.C., et al., *High-performance visible-light-driven SnS2/SnO2 nanocomposite photocatalyst prepared via in situ hydrothermal oxidation of SnS2 nanoparticles.* ACS applied materials & interfaces, 2011. **3**(5): p. 1528-1537.
18. Yao, K., et al., *One-step synthesis of urchinlike SnS/SnS2 heterostructures with superior visible-light photocatalytic performance.* Catalysis Communications, 2017. **101**: p. 51-56.
19. Burton, L.A., et al., *Synthesis, characterization, and electronic structure of single-crystal SnS, Sn2S3, and SnS2.* Chemistry of Materials, 2013. **25**(24): p. 4908-4916.
20. Ma, J., et al., *Designable fabrication of flower-like SnS 2 aggregates with excellent performance in lithium-ion batteries.* RSC Advances, 2012. **2**(9): p. 3615-3617.
21. Chaudhuri, T.K. and D. Tiwari, *Earth-abundant non-toxic Cu2ZnSnS4 thin films by direct liquid coating from metal–thiourea precursor solution.* Solar Energy Materials and Solar Cells, 2012. **101**: p. 46-50.
22. Yang, H., et al., *Nontoxic and abundant copper zinc tin sulfide nanocrystals for potential high-temperature thermoelectric energy harvesting.* Nano letters, 2012. **12**(2): p. 540-545.
23. An, X., C.Y. Jimmy, and J. Tang, *Biomolecule-assisted fabrication of copper doped SnS 2 nanosheet–reduced graphene oxide junctions with enhanced visible-light photocatalytic activity.* Journal of Materials Chemistry A, 2014. **2**(4): p. 1000-1005.
24. Lei, Y., et al., *Facile synthesis and assemblies of flowerlike SnS2 and In3+-doped SnS2: hierarchical structures and their enhanced photocatalytic property.* The Journal of Physical Chemistry C, 2009. **113**(4): p. 1280-1285.
25. Anderson, C. and A.J. Bard, *Improved photocatalytic activity and characterization of mixed TiO2/SiO2 and TiO2/Al2O3 materials.* The Journal of Physical Chemistry B, 1997. **101**(14): p. 2611-2616.
26. Zou, L., et al., *Removal of VOCs by photocatalysis process using adsorption enhanced TiO2–SiO2 catalyst.* Chemical Engineering and Processing: Process Intensification, 2006. **45**(11): p. 959-964.
27. Tang, W., et al., *Synthesis of a superparamagnetic MFNs@ SiO 2@ Ag 4 SiW 12 O 40/Ag composite photocatalyst, its superior photocatalytic performance under visible light illumination, and its easy magnetic separation.* RSC Advances, 2014. **4**(57): p. 30090-30099.
28. Fu, Y.Y., C.X. Yang, and X.P. Yan, *Fabrication of ZIF-8@ SiO2 Core–Shell Microspheres as the Stationary Phase for High-Performance Liquid Chromatography.* Chemistry-A European Journal, 2013. **19**(40): p. 13484-13491.
29. Wu, H.-S., et al., *Novel TiO 2–Pt@ SiO 2 nanocomposites with high photocatalytic activity.* Nanoscale, 2012. **4**(10): p. 3242-3247.
30. Zhu, S.-R., et al., *Hierarchical core–shell SiO 2@ PDA@ BiOBr microspheres with enhanced visible-light-driven photocatalytic performance.* Dalton Transactions, 2017. **46**(34): p. 11451-11458.
31. Xiong, Y., et al., *Ultra-sensitive NH3 sensor based on flower-shaped SnS2 nanostructures with sub-ppm detection ability.* Journal of hazardous materials, 2018. **341**: p. 159-167.
32. Mahesh, K. and D.-H. Kuo, *Synthesis of Ni nanoparticles decorated SiO2/TiO2 magnetic spheres for enhanced photocatalytic activity towards the degradation of azo dye.* Applied Surface Science, 2015. **357**: p. 433-438.

Preprints (www.preprints.org) | NOT PEER-REVIEWED | Posted: 3 April 2018 doi:10.20944/preprints201804.0036.v1

Peer-reviewed version available at *Materials* **2018**, *11*, 1030; doi:10.3390/ma11061030

33. Wei, R., et al., *Glutatione modified ultrathin SnS2 nanosheets with highly photocatalytic activity for wastewater treatment.* Materials Research Express, 2014. **1**(2): p. 025018.
34. Uma, K., et al., *The photodeposition of surface plasmon Ag metal on SiO2@ α-Fe2O3 nanocomposites sphere for enhancement of the photo-Fenton behavior.* Applied Surface Science, 2017. **425**: p. 377-383.
35. Huang, Y., et al., *Tin Disulfide 瑴 An Emerging Layered Metal Dichalcogenide Semiconductor: Materials Properties and Device Characteristics.* Acs Nano, 2014. **8**(10): p. 10743-10755.
36. He, M., L.-X. Yuan, and Y.-H. Huang, *Acetylene black incorporated three-dimensional porous SnS 2 nanoflowers with high performance for lithium storage.* RSC Advances, 2013. **3**(10): p. 3374-3383.
37. Pawar, R.C., et al., *Evaluation of a multi-dimensional hybrid photocatalyst for enrichment of H 2 evolution and elimination of dye/non-dye pollutants.* Catalysis Science & Technology, 2017. **7**(12): p. 2579-2590.